Polarized QED Cascades over Pulsar Polar Caps

Huai-Hang Song[1]★ † and Matteo Tamburini[2]‡

[1]*Institute of Physics, Chinese Academy of Sciences, Beijing 100190, China*
[2]*Max-Planck-Institut für Kernphysik, Saupfercheckweg 1, D-69117 Heidelberg, Germany*

ABSTRACT

The formation of $e^\pm$ plasmas within pulsar magnetospheres through quantum electrodynamics (QED) cascades in vacuum gaps is widely acknowledged. This paper aims to investigate the effect of photon polarization during the QED cascade occurring over the polar cap of a pulsar. We employ a Monte Carlo-based QED algorithm that accurately accounts for both spin and polarization effects during photon emission and pair production in both single-particle and particle-in-cell (PIC) simulations. Our findings reveal distinctive properties in the photon polarization of curvature radiation (CR) and synchrotron radiation (SR). CR photons exhibit high linear polarization parallel to the plane of the curved magnetic field lines, whereas SR photons, on average, demonstrate weak polarization. As the QED cascade progresses, SR photons gradually dominate over CR photons, thus reducing the average degree of photon polarization. Additionally, our study highlights an intriguing observation: the polarization of CR photons enhances $e^\pm$ pair production by approximately 5%, in contrast to the inhibition observed in laser-plasma interactions. Our self-consistent QED PIC simulations in the corotating frame reproduce the essential results obtained from single-particle simulations.

Key words: pulsar magnetosphere – QED cascade – electron-positron pair – gamma photon – spin and polarization effects

1 INTRODUCTION

Pulsars are commonly understood to be rotation-powered neutron stars, and treated as rotating magnetic dipoles characterized by superstrong magnetic fields at the 10^{12} G level close to their surface (Hewish et al. 1968; Gold 1968; Michel 1982; Philippov & Kramer 2022). In vacuum, the rapid rotation of pulsars would induce a strong electric field $E_\parallel$ aligned with the magnetic field. The force associated to this induced electric field can surpass the gravitational pull, leading to the extraction of charged particles from the pulsar surface. To resolve this issue, Goldreich & Julian (1969) proposed the presence of a magnetosphere surrounding the pulsar, comprising corotating plasmas that effectively screen the parallel electric field. These plasmas are thought to be $e^\pm$ plasmas sustained by quantum electrodynamics (QED) cascades, with the polar cap identified as one of the key regions for their occurrence (Sturrock 1971; Ruderman & Sutherland 1975; Arons & Scharlemann 1979).

The polarized QED cascade process over a pulsar polar cap is illustrated in Fig. 1. High-energy $e^\pm$, accelerated by the electric field, are confined to move along the curved magnetic field lines with minimal pitch angles, emitting γ photons through curvature radiation (CR). These emitted γ photons travel straight, leading to an increase in their propagation angles relative to the magnetic field lines until they decay into $e^\pm$ pairs. The created $e^\pm$ pairs, inheriting large pitch angles from their parent γ photons, undergo synchrotron radiation
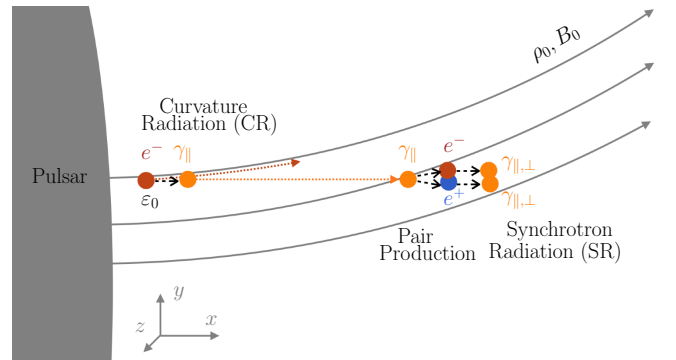

Figure 1. Schematic representation of the polarized QED cascade over a pulsar polar cap. High-energy $e^\pm$ particles, traversing the curved magnetic field, emit $\gamma_\parallel$ photons through CR, which subsequently convert into $e^\pm$ pairs. The resulting $e^\pm$ pairs can emit both $\gamma_\parallel$ and $\gamma_\perp$ photons via SR. The symbols $\gamma_\parallel$ and $\gamma_\perp$ denote photons polarized parallel and perpendicular to the plane of the magnetic field lines, respectively.

(SR) emission while simultaneously experiencing strong radiation reaction. Subsequently, SR photons with sufficient energy also decay into $e^\pm$ pairs. The unscreened parallel electric field $E_\parallel$ accelerates the created $e^\pm$ pairs, reducing their pitch angles and potentially bringing them into the CR regime. This cycle of photon emission and pair production sustains the QED cascade. Ultimately, the generated $e^\pm$ plasma becomes sufficiently dense to screen the parallel electric field $E_\parallel$, thus creating the pulsar magnetosphere and approaching a force-free environment.

★ Contact e-mail: huaihangsong@sjtu.edu.cn
† Present address: Key Laboratory for Laser Plasmas (MOE), School of Physics and Astronomy, Shanghai Jiao Tong University, Shanghai 200240, China
‡ Contact e-mail: Matteo.Tamburini@mpi-hd.mpg.de

Magnetohydrodynamics simulations (Spitkovsky 2006) and particle-in-cell (PIC) simulations based on heuristic QED models (Philippov & Spitkovsky 2014; Chen & Beloborodov 2014; Belyaev 2015; Cerutti et al. 2015; Kalapotharakos et al. 2018; Timokhin & Harding 2019; Cruz et al. 2022) have been conducted to replicate force-free pulsar magnetosphere features (Contopoulos et al. 1999). However, to accurately capture local dynamics like the QED cascade, first-principles QED-PIC simulations that incorporate precise rates of photon emission and pair production are essential. Previous 1D QED-PIC simulations in the corotating frame suggest that the QED cascade over the pulsar polar cap is dynamic, contrary to previous assumptions of stationarity (Timokhin 2010; Timokhin & Arons 2013). This nonstationary creation of $e^\pm$ plasmas may hold significance in explaining the origins of pulsar radio emission (Philippov et al. 2020; Cruz et al. 2021).

Prior QED-PIC simulations investigating QED cascades in a pulsar magnetosphere typically considered unpolarized photon emission and pair production rates, neglecting the effect of $e^\pm$ spin and γ photon polarization. With recent advancements in strong-field QED physics largely stimulated by the construction of PW-class laser facilities worldwide (Danson et al. 2019), there is a growing interest in $e^\pm$ spin and γ photon polarization effects in various contexts, particularly in laser-electron collisions and laser-plasma interactions (Li et al. 2019; Chen et al. 2019; Wen et al. 2019; Wan et al. 2020; Gong et al. 2021; Song et al. 2021b, 2022; Gong et al. 2023a,b). In a pulsar, the directionality of the slightly curved magnetic field above the pulsar polar cap implies the potential significance of spin and polarization effects for the development of QED cascades. In fact, the motion of $e^\pm$ is primarily along the magnetic field line, offering a unique perspective compared to studies in storage rings or lasers, where motion is predominantly perpendicular to the external field (Jackson 1976; Wan et al. 2020; Seipt et al. 2021; Song et al. 2021b). This suggests that QED cascades in pulsars may exhibit distinct spin or polarization properties.

In this paper, we employ a semiclassical Monte Carlo-based single-particle code and a first-principles QED PIC code that resolves $e^\pm$ spin and γ photon polarization to simulate the polarized QED cascade over a pulsar polar cap. Our simulation results show that emitted CR photons exhibit significant linear polarization parallel to the plane of the curved magnetic field line. This polarization arises from the $e^\pm$ acceleration, which determines the polarization of the emitted photons, being predominantly directed along the magnetic field plane. In contrast, the fast gyration motion of $e^\pm$ with nearly uniformly rotated acceleration directions results in a weak average polarization of SR photons. As CR photons, chiefly emitted by the primary $e^\pm$, are more energetic than SR photons, the average photon polarization increases with higher photon energy. The high degree of polarization of CR photons leads to a higher pair production rate compared to the unpolarized one, resulting in approximately 5% more $e^\pm$ pairs in simulations accounting for photon polarization. Both "shower-type" (S-type), i.e. without parallel electric field $E_\parallel$, and self-sustained "avalanche-type" (A-type), i.e. with $E_\parallel$, QED cascades exhibit similar features, with A-type cascades having a larger proportion of SR photons due to accelerated secondary $e^\pm$ pairs reaching higher energies. Fully 3D single-particle simulation results are confirmed by 1D QED-PIC simulations in the corotating frame.

The remaining sections of this paper are organized as follows. Section 2 provides an overview of the strong-field QED theory and simulation method utilized. In Section 3, we conduct a detailed analysis of photon polarization in three distinct radiation regimes using single-particle simulations. Section 4 delves into the comprehensive cascade of photon emission and pair production, employing both single-particle simulations and QED-PIC simulations. Specifically, we study the time evolution of photon emission and analyze the impact of polarization on pair production. Finally, Section 5 offers a concise summary of our key findings.

2 SIMULATION METHOD

Our implementation of polarized QED modules remains consistent across the single-particle and the QED-PIC codes. We utilize semiclassical spin- and polarization-resolved rates for photon emission and pair production in the locally-constant-field approximation (LCFA) (Ritus 1985; Baier et al. 1998). To preserve fully 3D polarization information, we choose the mean probability axis as the quantization axis (Yokoya 2011). A detailed algorithm description and benchmarking can be found in the work of one of the authors (Song et al. 2022). In this section, we summarize the aspects relevant for this study.

In accordance with the strong-field QED theory of polarization-dependent pair production (as outlined below), the velocity of primary particles responsible for CR emission is nearly aligned with the magnetic field lines. Consequently, the spin of the created $e^\pm$ pairs is essentially *perpendicular* to the direction of the magnetic field[1]. Hence, the fast spin precession of $e^\pm$ within the superstrong magnetic field of the pulsar results into a rapid depolarization. Indeed, in our fully spin- and polarized-resolved simulations, we observe no significant net $e^\pm$ spin polarization. Consequently, our focus shifts to the analysis of photon polarization. With resolved photon polarization, the semiclassical rates for photon emission and pair production in the LCFA can be written as (Baier et al. 1998)

$$\frac{dW_\gamma}{d\varepsilon_\gamma} = \frac{C_0 \Delta t}{\varepsilon_e^2}\left[\frac{\varepsilon_e^2 + \varepsilon_e'^2}{\varepsilon_e \varepsilon_e'}K_{\frac{2}{3}}(y_1) - \text{Int}K_{\frac{1}{3}}(y_1) + \xi_3 K_{\frac{2}{3}}(y_1)\right], \quad (1)$$

$$\frac{dW_\pm}{d\varepsilon_\pm} = \frac{C_0 \Delta t}{\varepsilon_\gamma^2}\left[\frac{\varepsilon_+^2 + \varepsilon_-^2}{\varepsilon_+ \varepsilon_-}K_{\frac{2}{3}}(y_2) + \text{Int}K_{\frac{1}{3}}(y_2) - \xi_3' K_{\frac{2}{3}}(y_2)\right], \quad (2)$$

where $C_0 = \alpha m_e^2 c^4/(2\sqrt{3}\pi\hbar)$, $K_\nu(y)$ is the modified Bessel function of the second kind with a non-integer ν, $\text{Int}K_{\frac{1}{3}}(y) \equiv \int_y^\infty K_{\frac{1}{3}}(x)\,dx$, m_e is the electron mass, c is the speed of light in vacuum, $\hbar$ is the reduced Planck constant, $\alpha \approx 1/137$ is the fine structure constant, and Δt is the time-step. In Eq. (1), ε_e and ε_e' are the $e^\pm$ energies before and after the photon emission, respectively, ε_γ the emitted photon energy, $\varepsilon_e' = \varepsilon_e - \varepsilon_\gamma$, and $y_1 = 2\varepsilon_\gamma/(3\varepsilon_e'\chi_e)$. In Eq. (2), $\varepsilon_\pm$ and ε_γ are the energies of the created $e^\pm$ pair and the decayed γ photon, respectively, and $y_2 = 2\varepsilon_\gamma^2/(3\chi_\gamma\varepsilon_+\varepsilon_-)$. Two strong-field QED parameters $\chi_e = (e\hbar/m_e^3 c^4)|F_{\mu\nu}p^\nu|$ and $\chi_\gamma = (e\hbar^2/m_e^3 c^4)|F_{\mu\nu}k^\nu|$ determine the importance of photon emission and pair production, with $\hbar k^\nu$ and p^ν being the photon and $e^\pm$ four-momentum, respectively. In our simulations, we set the momentum direction of generated particles and their parent particle to be collinear.

The Stokes vector, also referred to as photon polarization hereafter, $\boldsymbol{\xi} = (\xi_1, \xi_2, \xi_3)$ of the emitted photon in Eq. (1) is defined in the basis $(\boldsymbol{e}_1, \boldsymbol{e}_2, \boldsymbol{e}_v)$, where $\boldsymbol{e}_v$ is the unit vector along the photon velocity, $\boldsymbol{e}_1$ is the unit vector along the transverse acceleration of its

---

[1] This stands in stark contrast to scenarios such as storage rings or laser-plasma interactions, where the velocity of primary particles is typically transverse to the external field, and the spin of the created $e^\pm$ pairs is predominantly *aligned* with the external field.
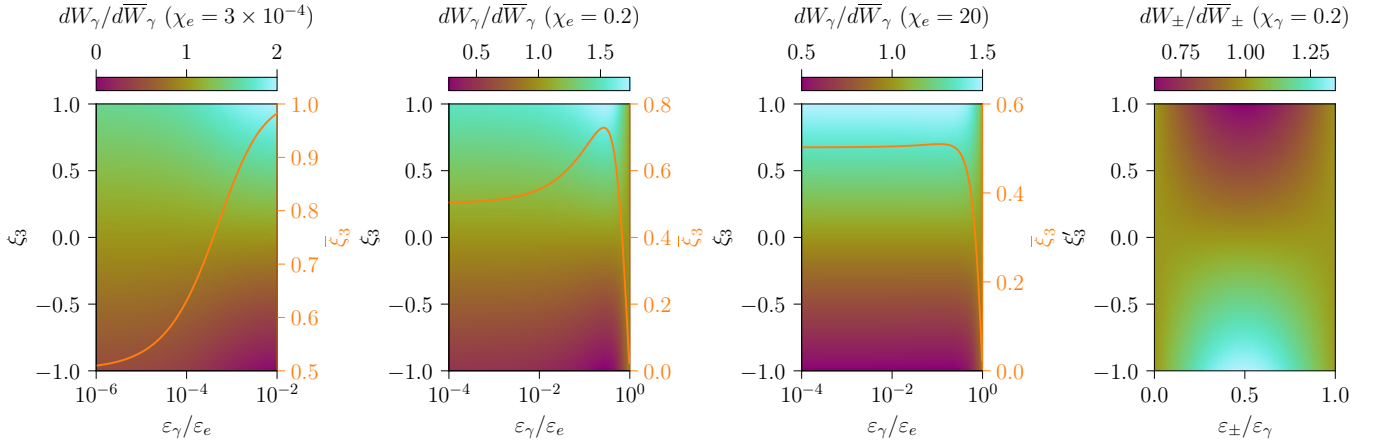
Figure 2. The normalized rates of photon emission, $W_\gamma/\overline{W}_\gamma$ (three left-most panels), and pair production, $W_\pm/\overline{W}_\pm$ (right-most panel), are calculated using Eqs.(1) and(2), where $\overline{W}_\gamma$ and $\overline{W}_\pm$ are the corresponding unpolarized rates. In the three left panels, the orange line illustrates the average photon polarization, $\overline{\xi}_3$, as a function of the photon energy ratio, $\varepsilon_\gamma/\varepsilon_e$. The QED parameters in these panels are set as $\chi_e = 3 \times 10^{-4}$, $\chi_e = 0.2$, and $\chi_e = 20$, while the right-most panel displays results with $\chi_\gamma = 0.2$. In the right-most panel, observe the symmetry with respect to the $\varepsilon_\gamma/\varepsilon_e = 0.5$ axis, and the increased probability of particle creation with $\xi'_3 < 0$.

parent $e^\pm$, and $e_2 = e_v \times e_1$. The positive (negative) value of the photon polarization $\xi_3 > 0$ ($\xi_3 < 0$) represents that photons are linearly polarized predominantly along the e_1 (e_2) direction. Another similar Stokes vector $\boldsymbol{\xi}' = (\xi'_1, \xi'_2, \xi'_3)$ in Eq. (2) is defined in another basis (e'_1, e'_2, e_v), where e'_1 is the unit vector along the transverse acceleration direction of the created positron, and $e'_2 = e_v \times e'_1$. Here, the photon Stokes vector describes a mixed state, with $|\boldsymbol{\xi}| \leqslant 1$, $|\boldsymbol{\xi}'| \leqslant 1$. In Eqs. (1) and (2), we have omitted the ξ_1 and ξ_2 components because they are zero on average in our case.

The two Stokes components ξ_3 and ξ'_3 in Eqs. (1) and (2) can be transformed into each other via (McMaster 1961)

$$\xi'_3 = \xi_3 \cos(2\phi), \tag{3}$$

where ϕ is the angle between the two transverse acceleration directions of e_1 and e'_1. If e_1 and e'_1 are collinear, then $\phi = 0$ or π, and $\xi'_3 = \xi_3$; otherwise, $\xi'_3 = -\xi_3$ if e_1 is perpendicular to e'_1. We will see that the latter case holds for CR photons.

The preferred polarization of emitted photons can be determined from Eq. (1). The polarized photon emission rates W_γ normalized to the unpolarized ones $\overline{W}_\gamma$ are displayed in the three left panels of Fig. 2. Three QED parameters $\chi_e = 3 \times 10^{-4}$, $\chi_e = 0.2$, and $\chi_e = 20$ are shown, which correspond to CR, SR, and super-SR (defined in the next section), respectively. For all three regimes, the normalized photon emission rate $W_\gamma/\overline{W}\gamma$ increases with the photon polarization ξ_3 for fixed photon energy. This indicates that the emitted photons with $\xi_3 > 0$ dominate, being mainly linearly polarized along the e_1 axis, i.e., the transverse acceleration axis. Note that since χ_e of CR is much smaller than 1, high-energy photons are still much less energetic than their parent $e^\pm$. In each panel, the average photon polarization $\overline{\xi}_3$ as a function of the photon energy ratio $\varepsilon_\gamma/\varepsilon_e$ is presented by the orange line. For CR, $\overline{\xi}_3$ grows from 0.5 at $\varepsilon_\gamma/\varepsilon_e \lesssim 10^{-6}$ to nearly 1 at $\varepsilon_\gamma/\varepsilon_e \approx 10^{-2}$. Thus, the highest energy CR photons are highly linearly polarized. For SR, where the emitted photons can take away most of the energy of their parent $e^\pm$, $\overline{\xi}_3$ also increases from roughly 0.5, reaching a maximum of about 0.7 at $\varepsilon_\gamma/\varepsilon_e \approx 0.3$ in the case of $\chi_e = 0.2$, and then drops to 0 when $\varepsilon_\gamma/\varepsilon_e$ approaches 1. This is because the photon polarization is highly sensitive to the spin polarization of their parent $e^\pm$ when the emitted

photon energy is close to the energy of the parent $e^\pm$. Therefore, the opposite result to CR photons is concluded: the highest energy SR photons are weakly polarized. For super-SR with a large χ_e, e.g., $\chi_e = 20$, the photon polarization peak at middle energies nearly disappears, leading to $\overline{\xi}_3$ almost monotonically decreasing from 0.5 to 0 with the increase of $\varepsilon_\gamma/\varepsilon_e$. Note that, as it will be clear below, super-SR often occurs for large values of χ_e, but does *not* coincide with $\chi_e \gg 1$.

Similarly, the pair production rate also depends on the polarization of parent photons according to Eq. (2). The right-most panel of Fig. 2 shows that the normalized pair production rate $W_\pm/\overline{W}_\pm$ decreases with the increase of ξ'_3 for a fixed $e^\pm$ energy, indicating that photons with $\xi'_3 < 0$ are more prone to decay into $e^\pm$ pairs. The effect of photon polarization on the pair production rate can be up to a maximum of about 30%, peaking at $\varepsilon_\gamma/\varepsilon_e = 0.5$ for $\chi_\gamma \lesssim 1$.

Note that the photon polarizations ξ_3 and ξ'_3 in Eqs. (1) and (2) are defined with respect to different axes, i.e., e_1 and e'_1, respectively. For convenience, hereafter, we use the same basis (e_y, e_z, e_x) for γ photons propagating along the assumed magnetic field direction e_x. Therefore, the positive (negative) value of ξ_3 represents linear photon polarization mainly along the e_y (e_z) direction.

3 PHOTON POLARIZATION

In this section, we focus on a clear comparison of the polarization between CR and SR photons. Specifically, we only consider photon emission within approximately one photon emission length, and pair production is neglected in simulations.

The polarization characteristics of CR and SR, often referred to as synchro-curvature radiation (Cheng & Zhang 1996; Viganò et al. 2015), can be analyzed in a unified manner by considering an electron beam with an initial energy ε_0 and pitch angle θ_0 injected into a purely curved magnetic field. In this case, we assume a simple field configuration where the magnetic field is predominantly directed along the $+e_x$ direction and slightly curved towards the $+e_y$ direction, with a constant magnitude of $B_0 = 4 \times 10^{11}$ G. To reduce computational costs, we adopt a constant curvature radius of $\rho_0 = 10$ km, which is smaller than the typical values (100–1000 km)
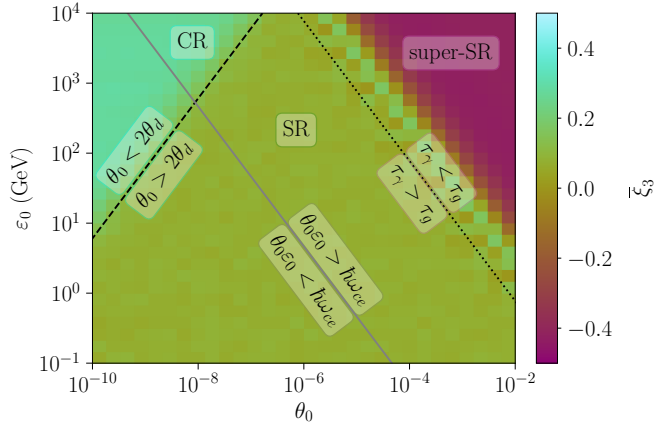
Figure 3. Simulation results reporting the average photon polarization $\overline{\xi}_3$ over a simulation duration equivalent to one photon emission length. The plot illustrates the dependence on the initial pitch angle, θ_0, and energy, ε_0, of the injected electron beam. Three distinct regimes – CR, SR, and super-SR – are demarcated by the dashed line $\theta_0 = 2\theta_d$ and the dotted line $\tau_\gamma = \tau_g$. Additionally, the solid line $\theta_0\varepsilon_0 = \hbar\omega_{ce}$ is presented, signaling the region where Landau energy quantization becomes essential.

but comparable to that of offset polar caps (Harding & Muslimov 2011). We set the initial pitch angle of the electron beam towards the $+e_y$ direction, specifically $\theta_y|_{t=0} = \theta_0$ and $\theta_z|_{t=0} = 0$, where $\theta_{y,z} = \arctan(p_{y,z}/|p_x|)$.

To confine the charged $e^\pm$ moving along the curved magnetic field, the net Lorentz force must act as a centripetal force, pointing from the $e^\pm$ position to the curvature center of the magnetic field line. The Lorentz force acting on $e^\pm$ is determined by its pitch angle. Therefore, the pitch angle θ of $e^\pm$ must be asymmetric about the magnetic field line during its propagation, a phenomenon known as drift velocity (Alfvén 1963). The center of the pitch angle in the θ_y-θ_z space will drift by $\theta_d = (\max|\theta_z| - \max|\theta_y|)$, which gives the the *drift angle* (Alfvén 1963)

$$\theta_d = \frac{\gamma_0 m_e c}{eB_0\rho_0} \approx 3.3 \times 10^{-9} \frac{\varepsilon_0(\text{TeV})}{B_0(10^{12}\,\text{G})\rho_0(10\,\text{km})}. \quad (4)$$

Photon emission attributed to CR occurs only for $e^\pm$ at small pitch angles $\theta \lesssim 2\theta_d$, while SR dominates if $\theta \gg 2\theta_d$. The defined boundary between these two mechanisms is essentially the same as that based on radiation power (Cheng & Zhang 1996; Viganò et al. 2015). This is because the radiation power is directly related to the QED parameter $\chi_e \approx \gamma_0\theta B_0/B_{cr}$, which is proportional to θ at $\theta \ll 1$, where $B_{cr} = m_e^2 c^2/e\hbar \approx 4.41 \times 10^{13}$ G is the QED critical strength of the magnetic field.

Finally, when considering photon polarization, a unique radiation regime, which we call *super-SR*, should be treated separately. This regime is characterized by a photon emission time $\tau_\gamma = 1/\int_0^{\varepsilon_e} d\varepsilon_\gamma (dW_\gamma/d\varepsilon_\gamma)$ smaller than the $e^\pm$ gyration period $\tau_g = 2\pi\gamma_0 m_e/eB_0$, corresponding to high $e^\pm$ energy and large pitch angle. To determine the boundary between the SR and super-SR regime, the photon emission time can be approximated as $\tau_\gamma \approx \hbar\gamma_0/(1.44\alpha m_e c^2 \chi_e)$ in the weak QED regime of $\chi_e \lesssim 1$ (Baier et al. 1998). The consistency of this approximation can be checked a posteriori (see below). Utilizing the small-angle approximation for χ_e, we obtain $\tau_\gamma \approx \hbar B_{cr}/(1.44\alpha m_e c^2 \theta B_0)$, which is independent of the particle's energy. The condition $\tau_\gamma < \tau_g$ yields $\gamma_0\theta > 1/(2.88\pi\alpha) \approx 15$, independent of the magnetic field strength. Using $\tau_\gamma = \tau_g$, the critical QED parameter at the boundary between

SR and super-SR is $\chi_e^{cr} = B_0/(2.88\pi\alpha B_{cr}) \approx 0.34 \times B_0(10^{12}\text{G})$, independent of the specific pitch angle and electron energy. For $B_0 \lesssim 10^{12}$G, this gives $\chi_e^{cr} \lesssim 0.1$, consistent with the initial assumption of the boundary between SR and super-SR being in the weak QED regime. Energetic super-SR photons are typically characterized by high linear polarization, but with the polarization direction *perpendicular* to that of CR photons.

In summary, the three different radiation regimes are

$$\begin{cases} \text{CR} : \theta < 2\theta_d; \\ \text{SR} : \theta > 2\theta_d \text{ and } \tau_\gamma > \tau_g; \\ \text{Super-SR} : \tau_\gamma < \tau_g. \end{cases} \quad (5)$$

To investigate photon polarization in the three radiation regimes, we conducted a series of 3D single-particle simulations, comprising 30×30 sets. The simulations involved logarithmic scans of the initial pitch angle θ_0, ranging from 10^{-10} to 10^{-2}, and electron energy ε_0, ranging from 100 MeV to 10 TeV. The numerical time step, Δt, was set to $10^{-4}\tau_\gamma$. Utilizing the Boris scheme for $e^\pm$ dynamics, we maintained accuracy in photon emission and CR photon polarization even with a relatively large time step, $\Delta t > \tau_g$ (Boris et al. 1970; Qin et al. 2013). In fact, test simulations performed by injecting a $\varepsilon_0 = 1$ TeV electron beam into the curved magnetic field of $B_0 = 4 \times 10^{11}$ G and $\rho_0 = 10$ km, and employing two time-steps $\Delta t = 10^{-6}$ ns and 10^{-3} ns showed no accumulation of numerical effects and small relative differences. The simulation outcomes, illustrating the average photon polarization $\overline{\xi}_3$ as a function of θ_0 and ε_0, are presented in Fig. 3. The sign of $\overline{\xi}_3$ effectively distinguishes three radiation regimes: $\overline{\xi}_3 > 0$ for CR, $\overline{\xi}_3 \approx 0$ for SR, and $\overline{\xi}_3 < 0$ for super-SR. It is worth noting that while Landau quantization is typically disregarded for magnetic field strengths $B_0/B_{cr} \lesssim 0.1$ (Harding & Preece 1987), The region characterized by very small pitch angles and low energies, defined by $\theta_0\varepsilon_0 < \hbar\omega_{ce}$, is forbidden due to Landau energy level quantization. Here, $\omega_{ce} = eB_0/m_e$ represents the nonrelativistic gyration frequency of an electron in the magnetic field. In the following, our discussion focuses on the parameter space where $\theta_0\varepsilon_0 \gg \hbar\omega_{ce}$. For better understanding, Fig. 4 illustrates three selected cases, each representing a distinct radiation regime.

(i) *CR*. With an initial pitch angle $\theta_0 = 10^{-8}$ and energy $\varepsilon_0 = 3$ TeV ($2\theta_d \approx 5.0 \times 10^{-8}$), the photon emission resides in the CR regime. Due to the magnetic field's curvature, the pitch angle is not symmetric about the field line; instead, its center shifts along the $-e_z$ direction by θ_d, as shown in the top-left panel of Fig. 4. Since the QED parameter χ_e, which determines the photon emission rate, is proportional to the pitch angle, most photons are emitted at $\theta_z < 0$. According to the polarized photon emission rate, photons are predominantly linearly polarized along the transverse acceleration direction of $e^\pm$. Consequently, on average CR photons are linearly polarized along the e_y direction, resulting in an average photon polarization $\overline{\xi}_3 > 0$ in the chosen basis (e_y, e_z, e_x). Consistent with the theoretical expectation, $\overline{\xi}_3$ monotonically increases with the photon energy.

(ii) *SR*. When the initial pitch angle is $\theta_0 = 10^{-6}$ and the energy is $\varepsilon_0 = 0.1$ TeV ($2\theta_d \approx 1.7 \times 10^{-9}$), and simultaneously the gyration period τ_g is smaller than the photon emission time τ_γ, the photon emission transitions into the SR regime. A notable difference from CR is that the pitch angle of SR is essentially symmetric about the magnetic field line in the θ_y-θ_z space, as shown in the middle-left panel of Fig. 4. Consequently, photons are nearly uniformly emitted during the $e^\pm$ gyration motion. Although photons remain linearly polarized along the azimuthal direction, i.e., the acceleration direction, the overall polarization at different pitch angles nearly
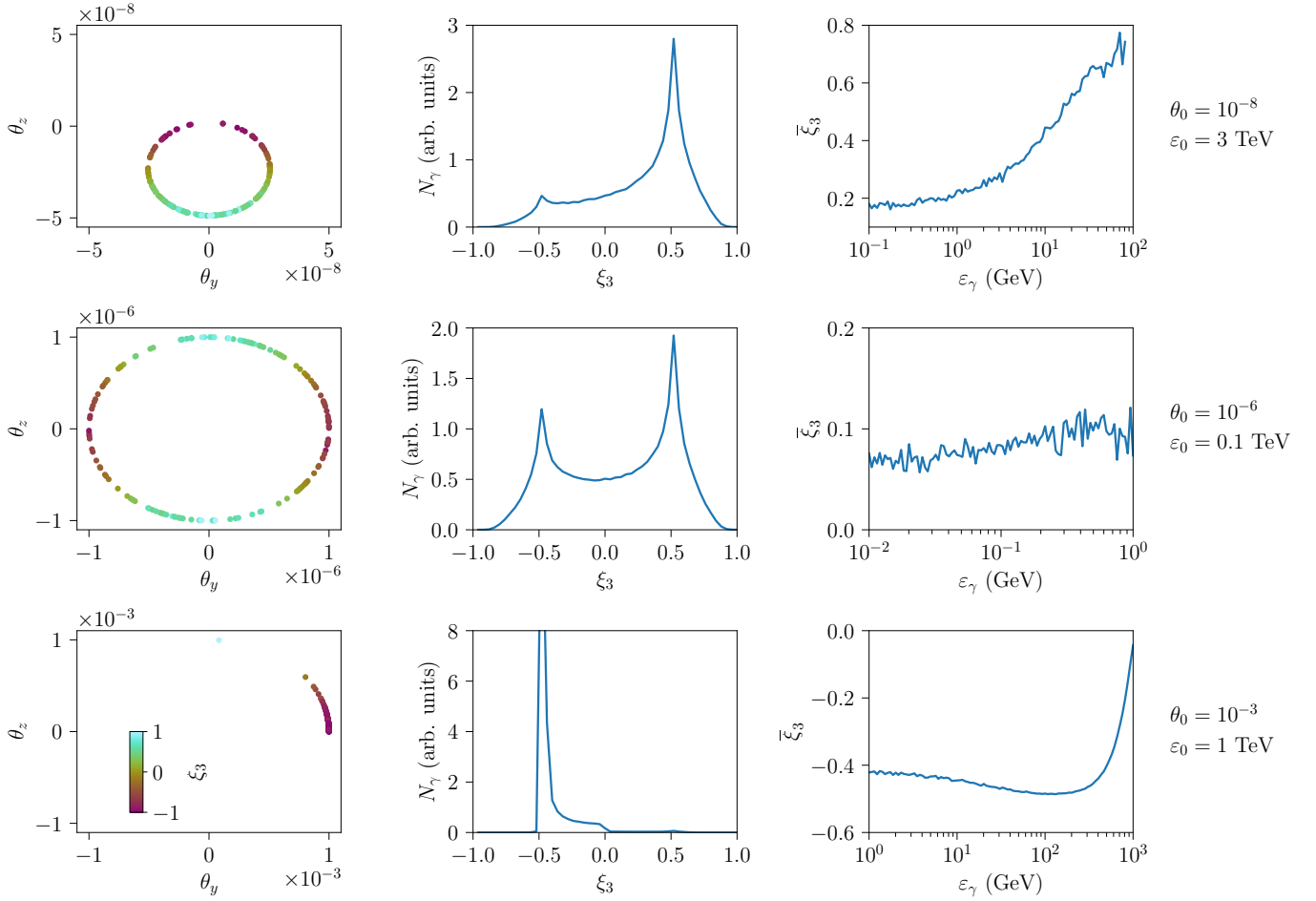
Figure 4. Comparison of photon polarizations in the CR $[\theta_0, \varepsilon_0] = [10^{-8}, 3\,\text{TeV}]$, SR $[\theta_0, \varepsilon_0] = [10^{-6}, 0.1\,\text{TeV}]$, and super-SR $[\theta_0, \varepsilon_0] = [10^{-3}, 1\,\text{TeV}]$ regimes. Left panels: the emitted photons versus their pitch angle components θ_y and θ_z at the emission time. The color represents the corresponding photon polarization ξ_3. Middle panels: the histograms of the photon polarization ξ_3. Right panels: the average photon polarization $\overline{\xi}_3$ as a function of the photon energy ε_γ.

cancels out. The curvature effect of the magnetic field induces a weak inhomogeneity of the photon emission in the $\boldsymbol{e}_z$ direction, leading to a slight dominance of $\xi_3 > 0$ photons. The average polarization $\overline{\xi}_3$ for all photons is approximately 8%, considerably smaller than the CR polarization degree and almost insensitive to the photon energy. Thus, for computational convenience, we treat SR photons as weakly polarized and directly set the polarization of all SR photons to a constant value of 8% in our subsequent simulations, which allows us to use a numerical time-step larger than the gyration period.

(iii) *Super-SR*. For $e^\pm$ with both large pitch angles and high energies ($\theta_0 = 10^{-3}$ and $\varepsilon_0 = 1\,\text{TeV}$, $2\theta_d \approx 1.7 \times 10^{-8}$), they are likely to emit photons on timescales shorter than the gyration period, simultaneously losing most of their energies due to radiation reaction. In this super-SR regime, photon emission concentrates near the initial $e^\pm$ position on the $+\boldsymbol{e}_y$ axis, as shown in the bottom-left panel of Fig. 4. Consequently, the emitted photons exhibit a distinct linear polarization directed perpendicular to the plane of magnetic field lines, i.e., $\overline{\xi}_3 < 0$. This is markedly different from the CR and SR regimes. The polarization degree of super-SR photons decreases to zero at high energy, in agreement with the theoretical expectation for $\chi_e > 1$. However, as we will see below, the existence of this super-SR regime is unlikely for $B_0 \gtrsim 4 \times 10^{11}$ G. This is because

a relatively large pitch angle corresponds to newly created $e^\pm$ pairs, which typically do not possess sufficient energy to emit in the super-SR regime. Consequently, this unique radiation regime will not be further detailed in this work.

4 POLARIZED QED CASCADE

In this section, we investigate the complete process of the polarized QED cascade by considering both photon emission and pair production. Our study encompasses single-particle simulations involving S-type and A-type cascades, with static external fields, as well as first-principles PIC simulations where the parallel electric field is self-consistently incorporated.

4.1 S-type QED cascades

We first study the S-type QED cascade initiated by an energetic electron beam in a pure magnetic field through single-particle simulations. We consider a monoenergetic electron beam with various initial energies, specifically $\varepsilon_0 = 2\,\text{TeV}$, 3 TeV, and 4 TeV, tangentially injected into the curved magnetic field. The magnetic field
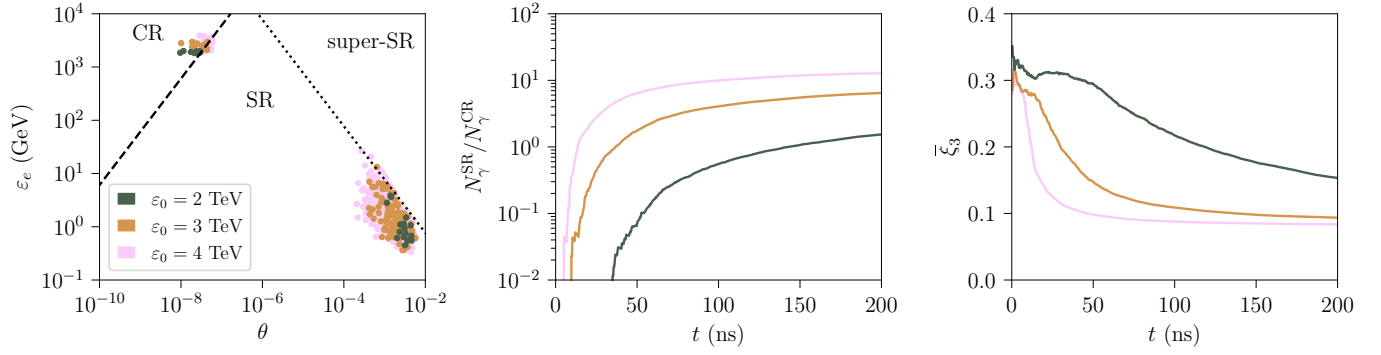
Figure 5. Single-particle simulation results of the S-type cascade for three values of the initial electron beam energy ε_0 = 2 TeV, 3 TeV, and 4 TeV. Left panel: the emitted photons in the θ-ε_e space. Middle panel: temporal evolution of the ratio $N_\gamma^{\mathrm{SR}}/N_\gamma^{\mathrm{CR}}$ between the number of SR photons and CR photons. Right panel: temporal evolution of the average photon polarization $\overline{\xi}_3$.
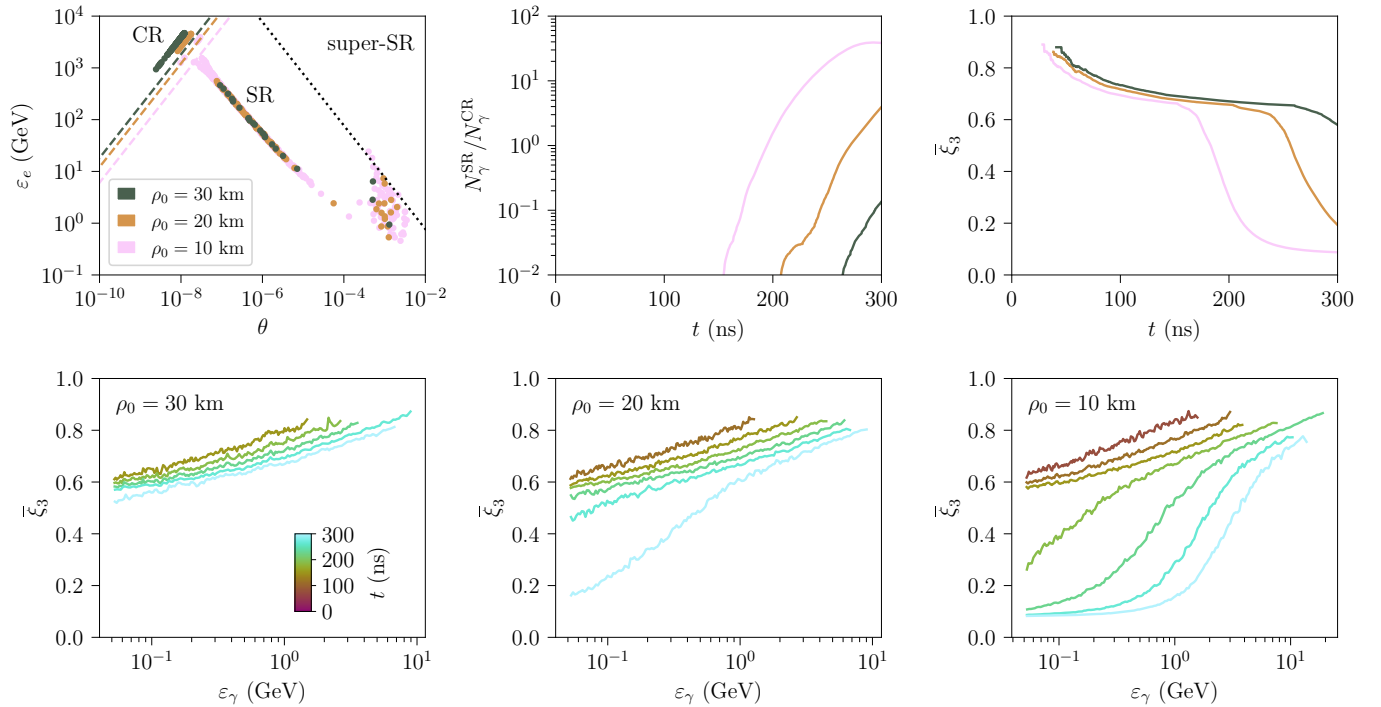

Figure 6. Top panels: the same plots as in Fig. 5 but for the A-type cascade with electrons initially at rest and for three choices of the magnetic field curvature radius, specifically ρ_0 = 10 km, 20 km, and 30 km. Dashed, matching the respective colors, delineate boundary lines ($\theta = 2\theta_d$) indicating CR and SR regimes. Bottom panels: the temporal evolution of the average photon polarization $\overline{\xi}_3$ versus the photon energy ε_γ across three distinct cases.

parameters align with those in section 3, with $B_0 = 4 \times 10^{11}$ G and $\rho_0 = 10$ km. In our simulations, the numerical time-step Δt is set to be 3.3×10^{-4} ns, which proves sufficient to resolve the dynamics for our cases.

From the simulation results reported in Fig. 5, we can effectively distinguish the emitted CR and SR photons in the θ-ε_e space for all three initial electron energies ε_0. As a reminder, θ and ε_e represent the pitch angle and energy of the emitting $e^\pm$, respectively. CR photons emerge from injected electrons of high energies ($\varepsilon_e \sim$ TeV) and small pitch angles ($\theta \sim 10^{-8}$–10^{-7}). On the other hand, SR photons originate from created secondary $e^\pm$ pairs with relatively lower energies ($\varepsilon_e \sim$ GeV) and larger pitch angles ($\theta \sim 10^{-4}$–10^{-2}). The maximum pitch angle of CR equals twice the drift angle θ_d as defined

in Eq. (4). As ε_0 increases, the pitch angle of SR decreases, because higher-energy CR photons can decay into $e^\pm$ pairs with smaller pitch angles. SR photons lie below the boundary line $\tau_\gamma = \tau_g$ of the super-SR regime, resulting in globally weak polarization.

As the QED cascade develops, the proportion of SR photons grows, eventually surpassing CR photons. This trend is evident in the temporal evolution of the number ratio of SR photons to CR photons, $N_\gamma^{\mathrm{SR}}/N_\gamma^{\mathrm{CR}}$ (see the middle panel of Fig. 5). The growth rate of $N_\gamma^{\mathrm{SR}}/N_\gamma^{\mathrm{CR}}$ exhibits significant variability with the initial electron energy ε_0, increasing much more rapidly with a larger ε_0. At the final simulation time t = 200 ns, $N_\gamma^{\mathrm{SR}} \approx N_\gamma^{\mathrm{CR}}$ for ε_0 = 2 TeV, while $N_\gamma^{\mathrm{SR}} \gg N_\gamma^{\mathrm{CR}}$ for both ε_0 = 3 TeV and 4 TeV. The weakly polarized SR photons emitted later contribute to the decrease in the average

photon polarization $\bar{\xi}_3$, depending also on the initial electron energy ε_0 (see the right panel of Fig. 5). For $\varepsilon_0 = 2$ TeV, the effects of pair production are relatively weak, leading to a decrease in average photon polarization from 30% to 15%. For lower energies, $\bar{\xi}_3$ rapidly decreases until it converges to a weak SR photon polarization of about 8%.

4.2 A-type QED cascade

To comprehensively explore the polarized QED cascade, we extend our investigation to include the A-type cascade by incorporating the $e^{\pm}$ acceleration process. In this scenario, an electron beam initially at rest experiences a strong parallel electric field $E_{\parallel}$ along the magnetic field direction. We set the constant electric field as $E_{\parallel} = 5 \times 10^{10}$ V/m, consistent with the values obtained from PIC simulations (see below). The magnetic field strength remains fixed at $B_0 = 4 \times 10^{11}$ G, and we consider three curvature radii, $\rho_0 = 10$ km, 20 km, and 30 km.

In the top-left panel of Fig. 6, we report the emitted photons in the θ-ε_e space under three curvature radii at the time $t = 300$ ns. Unlike the S-type cascade, the low-energy $e^{\pm}$ pairs created here are accelerated to higher energies by the parallel electric field. Consequently, in addition to CR photons from initial electrons ($\theta < 10^{-8}$) and SR photons from created $e^{\pm}$ pairs ($\theta > 10^{-4}$), we observe additional SR photons emitted by the accelerated $e^{\pm}$ pairs with small pitch angles ($10^{-8} < \theta < 10^{-4}$). As in the S-type cascade, super-SR photons are notably absent in all cases.

For the largest curvature radius $\rho_0 = 30$ km, the QED cascade evolves slowly, with pair production and consequently SR emission occurring toward the end of the simulation. The reduction in photon polarization over time is evident across the entire photon energy range, as depicted in the bottom-left panel of Fig. 6. For the smallest curvature radius $\rho_0 = 10$ km, at $t = 300$ ns SR photons have already outnumbered CR photons. The average photon polarization $\bar{\xi}_3$ decreases over time until it stabilizes at about 8%. The net polarization of low-energy photons experiences a rapid decline, while high-energy photons maintain a noticeably higher level of polarization, as illustrated in the bottom-right panel of Fig. 6. This is attributed to CR photons, which are highly polarized, having higher energies than SR photons, which are weakly polarized. Therefore, low-energy photons mainly undergo depolarization because of SR emissions. For the intermediate curvature radius, $\rho_0 = 20$ km, the QED cascade is still rapidly developing at $t = 300$ ns, exhibiting polarization characteristics between the cases of $\rho_0 = 10$ km and $\rho_0 = 30$ km.

4.3 Photon polarization effect on pair production

In this subsection, we investigate the influence of photon polarization on pair production. According to Eq. (2), the photon polarization can affect the pair production rate by as much as 30%. When applying Eq. (2), one should pay particular attention to the selected basis for the photon Stokes vector $\boldsymbol{\xi}$. The two basis vectors $\boldsymbol{e}_1$ in Eq. (1) and $\boldsymbol{e}'_1$ of pair production in Eq. (2) are mutually perpendicular for CR. This arises from the fact that the acceleration direction of $e^{\pm}$ in CR is mainly parallel to the plane of magnetic field lines, while for newly created $e^{\pm}$ pairs, the acceleration direction is mainly perpendicular to it. Consequently, this results in $\xi_3 \approx -\xi'_3$. From Eq. (2), the specific polarization of CR photons leads to a higher pair production rate compared to unpolarized photons. This finding starkly contrasts with results obtained in laser fields, where the photon polarization effect was observed to suppress pair production (Wan et al. 2020;
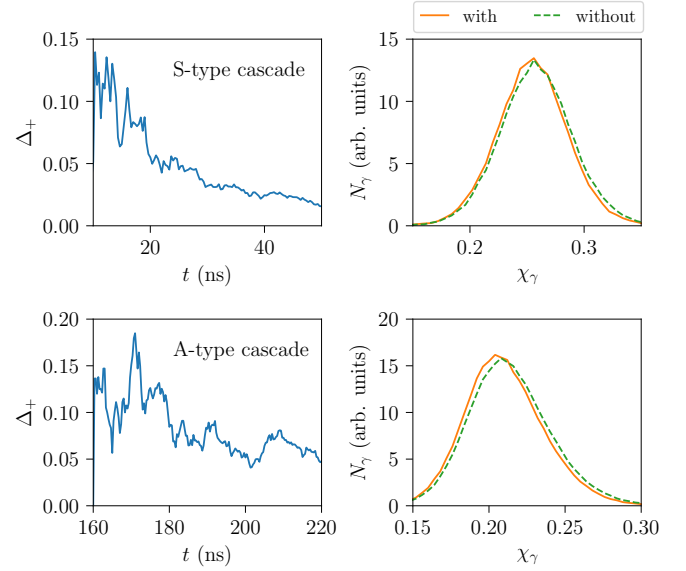

Figure 7. Left panels: the temporal evolution of the relative difference of the positron number $\Delta_+ = (N_+ - \overline{N}_+)/\overline{N}_+$, where N_+ and $\overline{N}_+$ are the number of generated positrons with and without considering the photon polarization, respectively. Right panels: the QED parameter χ_γ of decayed photons with and without the photon polarization. Top panel: S-type cascade with $\varepsilon_0 = 3$ TeV and other parameters the same as Fig. 5. Bottom panel: A-type cascade with $\rho = 10$ km and other parameters the same as Fig. 6.

Seipt et al. 2021; Song et al. 2021b). In fact, in laser fields, highly polarized photons are emitted via a SR-like mechanism, leading to $\xi_3 \approx \xi'_3$.

The relative difference in the positron number $\Delta_+ = (N_+ - \overline{N}_+)/\overline{N}_+$ between polarized and unpolarized results is reported in Fig. 7, where N_+ and $\overline{N}_+$ are the number of generated positrons with and without considering the photon polarization, respectively. Fig. 7 reveals that the number of created positrons is enhanced by more than 10% at the initial stage of the cascade due to the high polarization of CR photons. In the S-type cascade, at later times the relative difference narrows to less than 5%, even though the polarization of CR photons remains high. The comparison of the χ_γ of decayed photons with versus without photon polarization (see the right column of Fig. 7) reveals that for the unpolarized case, χ_γ at photon decay is slightly larger than in the polarized case. In fact, unpolarized photons with the same energy as polarized photons posses smaller decay rates and travel longer distances, thus acquiring larger pitch angles, and consequently slightly larger χ_γ than polarized photons before decaying into pairs. In the A-type cascade, photon polarization has a similar effect on pair production, as illustrated in the bottom panel of Fig. 7. The relative difference Δ_+ can exceed 10% at the initial stage and is also reduced to about 5% with the development of the QED cascade. Similar to the S-type cascade, a slight difference in χ_γ is observed between polarized and unpolarized results. At a later stage, a key factor to the reduction in the pair yield difference between polarized and unpolarized photons is the domination of unpolarized SR photons over polarized CR photons.

4.4 Polarized QED-PIC simulations

In our final set of simulations, we employ first-principles 1D (1D geometry but fully 3D particle momentum) QED-PIC simulations
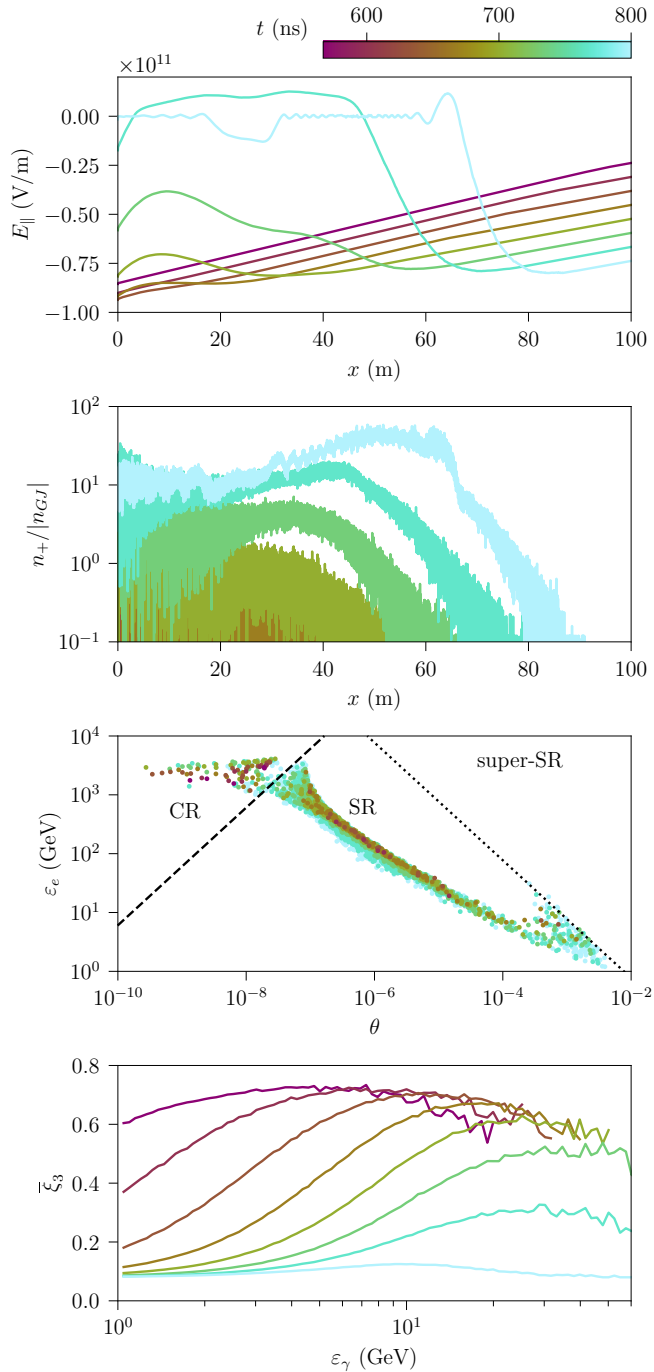
Figure 8. From top to bottom panel: Spatial distributions of the parallel electric field E_x and the normalized positron density $n_+/|n_{GJ}|$. Emitted γ photons in the θ-ε_e space. Temporal evolution of the photon polarization $\overline{\xi}_3$ in relation to the photon energy ε_γ.

in the corotating frame using the YUNIC code (Song et al. 2021a). YUNIC is a relativistic PIC code that includes polarized QED modules and has been previously utilized for studying polarized QED cascades in laser-plasma interactions (Song et al. 2021b, 2022). Notably, the electric field in these simulations is inhomogeneous and self-consistently solved. This is a crucial distinction from the single-particle simulations, where the electric field is not evolving. Here the electric field is excited by the outflow of charged $e^\pm$ plasmas

and subsequently screened by the created dense $e^\pm$ plasmas, all of which can be captured by the QED-PIC simulation. Our simulation setup is similar to the pioneering work (Timokhin 2010). There are several improvements in our QED-PIC code, in which a standard Monte-Carlo QED method developed in recent years by the laser-plasma community is adopted (Elkina et al. 2011; Gonoskov et al. 2015; Ridgers et al. 2014; Tamburini et al. 2017; Montefiori & Tamburini 2023), and enriched with the polarization effects introduced in section 2.

In the corotating frame, the governing Goldreich-Julian (GJ) equations are expressed as (Goldreich & Julian 1969; Timokhin 2010)

$$\nabla \times \boldsymbol{E} = 4\pi(n - n_{GJ}), \qquad \frac{\partial \boldsymbol{E}}{\partial t} = -4\pi(\boldsymbol{j} - \boldsymbol{j}_m). \qquad (6)$$

Initially, to satisfy Eq. (6), we set the net charge density $n|_{t=0}$ to be the GJ density $n_{GJ} = -\boldsymbol{\Omega}_0 \cdot \boldsymbol{B}/2\pi c$ and the net current density $\boldsymbol{j}|_{t=0}$ to be $\boldsymbol{j}_m$. Assuming the angular velocity $\boldsymbol{\Omega}_0$ of the pulsar rotation (rotation period $P_0 = 1$ s) is parallel to its magnetic moment, i.e., $n_{GJ} < 0$, the vacuum gap is closed with $\boldsymbol{E}|_{t=0} = 0$ at the beginning of the simulation. As the $e^\pm$ particles flow away from the simulation zone, Eq. (6) implies that a strong parallel electric field $E_\parallel$ is excited, accelerating $e^\pm$ and triggering the QED cascade.

Simulating the entire QED cascade from the vacuum gap closing to its opening and closing again is challenging due to the exponential growth in particle number. While particle merging methods can alleviate computational pressure, computational particle division only in the position-momentum space might result into loss of polarization information. Thus, we decided to avoid using particle merging, and limited ourselves to simulate the early stage of the QED cascade. Nonetheless, the created $e^\pm$ plasma at the end of the simulation is already dense enough to screen the excited electric field. Thus, the obtained PIC simulation results are representative of a well-developed QED cascade. Specifically, we set the initial charge densities of electrons and positrons to be $n_-|_{t=0} = 2n_{GJ}$ and $n_+|_{t=0} = -n_{GJ}$, respectively, and their initial current densities to be $\boldsymbol{j}_-|_{t=0} = \boldsymbol{j}_m = cn_{GJ}$ and $\boldsymbol{j}_+|_{t=0} = 0$. The total simulation box is $L_x = 120$ m, with each cell resolved by $d_x = 1/384$ m and initially filled with 10 electrons and 10 positrons. Absorbing boundaries are applied at both left and right sides, and no $e^\pm$ is supplied from the boundaries, which is similar to the "anti-GJ" space-charge limited flow (Beloborodov 2008; Timokhin 2010).

With the propagation of the initial flow of $e^\pm$ outside the computational box, a parallel electric field is excited, linearly increasing towards the pulsar surface (left boundary) to accelerate $e^\pm$ to high energies (see the top panel of Fig. 8). When the QED cascade starts, the density of created $e^\pm$ plasma near the pulsar surface can reach 30 times the GJ density at $t = 800$ ns, as shown in the second panel from the top of Fig. 8. As expected, the QED cascade creates large amounts of charges that screen the electric field and close the vacuum gap. The θ-ε_e space of photons at three different instants is displayed in the third panel from top of Fig. 8. Similar to the single-particle simulation results, CR photons have high energies and small pitch angles, while SR photons exhibit opposite features with lower energies and larger pitch angles than CR photons. The transition from primarily having CR photons to SR photons becoming dominant over time is evident. The average photon polarization $\overline{\xi}_3$ as a function of the emitted photon energy is shown in the bottom panel of Fig. 8, with the net polarization of low-energy photons gradually reducing due to the growth of the number of weakly polarized SR photons. An additional insight from the PIC simulation is that high-energy photons are also depolarized at a later stage. This is due to the strong induced electric field, which can accelerate a substantial fraction of secondary $e^\pm$ to

high energies. Before the electric field is screened, these accelerated $e^{\pm}$ emit high-energy photons while remaining in the SR regime. Despite their high energy, these SR photons are comparatively weakly polarized compared to CR photons. With the inclusion of photon polarization effects, we observe an enhancement of approximately 5% in the $e^{\pm}$ yield compared to the unpolarized results.

5 SUMMARY

In this paper, our investigation has centered on the polarized QED cascade occurring over the polar cap of a pulsar, with a primary focus on the polarization properties of photons in different radiation regimes. Our simulation tools include a 3D single-particle code and a 1D QED-PIC code, both previously employed in laser-beam and laser-plasma studies. While the former does not consider field evolution, the latter can self-consistently handle it. In both codes, we implement the same Monte Carlo QED module based on LCFA to calculate two nonlinear QED processes: γ photon emission and $e^{\pm}$ pair production. Notably, our QED module includes polarization calculations for both $e^{\pm}$ spin and γ photon polarization. However, due to the rapid spin precession, $e^{\pm}$ quickly depolarize, leading us to focus solely on the photon polarization effect.

Our results reveal distinct polarization properties of curvature radiation (CR) and synchrotron radiation (SR) photons. CR results in highly polarized photons in the plane of curved magnetic field lines. In contrast, SR photons are weakly polarized. The boundary between CR and SR regimes can be effectively defined by the pitch angle θ of emitting $e^{\pm}$, where $\theta < 2\theta_d$ corresponds to CR and $\theta > 2\theta_d$ to SR. Here, θ_d, defined in Eq. (4), represents the drift angle.

A series of 3D single-particle simulations explored the complete cascade of photon emission and pair production, encompassing both "shower-type" (S-type) and self-sustained "avalanche-type" (A-type). Initially, only CR photons, which posses a high degree of polarization, are emitted by injected electrons, but as the QED cascade progress, SR photons from secondary $e^{\pm}$ pairs gradually dominate, thus reducing the net average polarization. Furthermore, photon polarization influences pair production, with the high polarization of CR photons enhancing pair production by approximately 5% with respect to unpolarized simulations.

Finally, 1D QED-PIC simulations in the corotating frame confirm the robustness of our results against specific electric field forms, showcasing good agreement with single-particle simulations. This comprehensive approach provides valuable insights into the polarized QED cascade dynamics over a pulsar polar cap.

ACKNOWLEDGEMENTS

DATA AVAILABILITY

The data underlying this article will be shared on reasonable request to H.-H. Song.

REFERENCES

Alfvén H., 1963, Cosmical Electrodynamics. Clarendon Press
Arons J., Scharlemann E. T., 1979, Astrophys. J., 231, 854
Baier V. N., Katkov V., Strakhovenko V. M., 1998, Electromagnetic Processes at High Energies in Oriented Single Crystals. World Scientific, Singapore
Beloborodov A. M., 2008, Astrophys. J., 683, L41
Belyaev M. A., 2015, Mon. Not. R. Astron. Soc., 449, 2759
Boris J. P., et al., 1970, in Proc. Fourth Conf. Num. Sim. Plasmas. pp 3–67
Cerutti B., Philippov A., Parfrey K., Spitkovsky A., 2015, Mon. Not. R. Astron. Soc., 448, 606
Chen A. Y., Beloborodov A. M., 2014, Astrophys. J. Lett., 795, L22
Chen Y.-Y., He P.-L., Shaisultanov R., Hatsagortsyan K. Z., Keitel C. H., 2019, Phys. Rev. Lett., 123, 174801
Cheng K. S., Zhang J. L., 1996, Astrophys. J., 463, 271
Contopoulos I., Kazanas D., Fendt C., 1999, Astrophys. J., 511, 351
Cruz F., Grismayer T., Chen A. Y., Spitkovsky A., Silva L. O., 2021, Astrophys. J. Lett., 919, L4
Cruz F., Grismayer T., Iteanu S., Tortone P., Silva L. O., 2022, Phys. Plasmas, 29, 052902
Danson C. N., et al., 2019, High Power Laser Sci. Eng., 7, e54
Elkina N. V., Fedotov A. M., Kostyukov I. Y., Legkov M. V., Narozhny N. B., Nerush E. N., Ruhl H., 2011, Phys. Rev. ST Accel. Beams, 14, 054401
Gold T., 1968, Nature, 218, 731
Goldreich P., Julian W. H., 1969, Astrophys. J., 157, 869
Gong Z., Hatsagortsyan K. Z., Keitel C. H., 2021, Phys. Rev. Lett., 127, 165002
Gong Z., Hatsagortsyan K. Z., Keitel C. H., 2023a, Phys. Rev. Lett., 130, 015101
Gong Z., Shen X., Hatsagortsyan K. Z., Keitel C. H., 2023b, Phys. Rev. Lett., 131, 225101
Gonoskov A., et al., 2015, Phys. Rev. E, 92, 023305
Harding A. K., Muslimov A. G., 2011, Astrophys. J., 743, 181
Harding A. K., Preece R., 1987, Astrophys. J., 319, 939
Hewish A., Bell S. J., Pilkington J. D. H., Scott P. F., Collins R. A., 1968, Nature, 217, 709
Jackson J. D., 1976, Rev. Mod. Phys., 48, 417
Kalapotharakos C., Brambilla G., Timokhin A., Harding A. K., Kazanas D., 2018, Astrophys. J., 857, 44
Li Y.-F., Shaisultanov R., Hatsagortsyan K. Z., Wan F., Keitel C. H., Li J.-X., 2019, Phys. Rev. Lett., 122, 154801
McMaster W. H., 1961, Rev. Mod. Phys., 33, 8
Michel F. C., 1982, Rev. Mod. Phys., 54, 1
Montefiori S., Tamburini M., 2023, Comput. Phys. Commun., 292, 108855
Philippov A., Kramer M., 2022, Annu. Rev. Astron. Astrophys., 60, 495
Philippov A. A., Spitkovsky A., 2014, Astrophys. J. Lett., 785, L33
Philippov A., Timokhin A., Spitkovsky A., 2020, Phys. Rev. Lett., 124, 245101
Qin H., Zhang S., Xiao J., Liu J., Sun Y., Tang W. M., 2013, Phys. Plasmas, 20, 084503
Ridgers C., Kirk J., Duclous R., Blackburn T., Brady C., Bennett K., Arber T., Bell A., 2014, J. Comput. Phys., 260, 273
Ritus V. I., 1985, J. Sov. Laser Res., 6, 497
Ruderman M. A., Sutherland P. G., 1975, Astrophys. J., 196, 51
Seipt D., Ridgers C. P., Sorbo D. D., Thomas A. G. R., 2021, New J. Phys., 23, 053025
Song H.-H., Wang W.-M., Li Y.-T., 2021a (arXiv:2104.00642)
Song H.-H., Wang W.-M., Li Y.-F., Li B.-J., Li Y.-T., Sheng Z.-M., Chen L.-M., Zhang J., 2021b, New J. Phys., 23, 075005
Song H.-H., Wang W.-M., Li Y.-T., 2022, Phys. Rev. Lett., 129, 035001
Spitkovsky A., 2006, Astrophys. J., 648, L51
Sturrock P. A., 1971, Astrophys. J., 164, 529
Tamburini M., Di Piazza A., Keitel C. H., 2017, Sci. Rep., 7, 5694
Timokhin A. N., 2010, Mon. Not. R. Astron. Soc., 408, 2092
Timokhin A. N., Arons J., 2013, Mon. Not. R. Astron. Soc., 429, 20
Timokhin A. N., Harding A. K., 2019, The Astrophys. J., 871, 12
Viganò D., Torres D. F., Hirotani K., Pessah M. E., 2015, Mon. Not. R. Astron. Soc., 447, 1164
Wan F., et al., 2020, Phys. Rev. Research, 2, 032049

Wen M., Tamburini M., Keitel C. H., 2019, Phys. Rev. Lett., 122, 214801
Yokoya K., 2011, User's Manual of CAIN Version 2.42

This paper has been typeset from a TEX/LATEX file prepared by the author.